Experimental validation of a topology optimized 2D sandwich panel for sound transmission minimization

Vanessa Cool[a,c], Claus Claeys[a,c], Hervé Denayer[a,c], Frank Naets[a,c], Elke Deckers[b,c]

[a] *KU Leuven, Department of Mechanical Engineering, Division LMSD, Celestijnenlaan 300 - box 2420, Heverlee, Belgium*
[b] *KU Leuven Campus Diepenbeek, Department of Mechanical Engineering, Wetenschapspark 27, 3590 Diepenbeek, Belgium*
[c] *Flanders Make@KU Leuven, Belgium*

Abstract

In industry, an increasing pressure is perceived to obtain dynamical systems which are light-weight, load-carrying and achieve excellent noise and vibration properties. Sandwich panels with specifically designed structural-acoustic cores have shown potential to reconcile these conflicting requirements. Optimization techniques can be used to automate the design process while making a trade-off between the conflicting requirements. This work proposes a methodology to easily validate the sound transmission loss (STL) of 2D structures. The experimental validation considers a thin slice of the extruded 2D topology as an input and by a purely structural excitation and measurement, the STL is obtained. This enables a fast validation of novel sandwich core designs without the need to go to 3D simulations, fabrication and measurements. In this manuscript, the experimental validation is demonstrated for a sandwich core design coming out of a topology optimization framework which achieves a high STL by a mode-conversion effect. The methodology can equally well be applied to validate a 2D design obtained via other strategies. The near-2D finite sample is fabricated, tested and compared to two reference cases being the equivalent mass and double mass case. These two cases are selected to show the performance of the optimized design while still being lightweight. An excellent match is achieved between the numerically and experimentally obtained STL performance for the specific design considered, demonstrating the validity of the experimental validation technique and confirming the mode-conversion effect to achieve high STL.

Keywords: Topology Optimization, Sound Transmission Loss, Experimental validation

1. Introduction

Light-weight, self-supporting and good noise, vibration and harshness (NVH) properties, those are the three conflicting requirements dynamical systems often need to comply to nowadays. To achieve this, innovative structures are needed that make a trade-off between the different requirements. Over the past decades, sandwich panels have shown

Email address: vanessa.cool@kuleuven.be (Vanessa Cool)

their potential in achieving this compromise in a wide range of applications, ranging from aerospace to construction industry. Depending on the targeted requirements, the nature of sandwich panel core differs. Sandwich panels with air or foam cores target superior sound transmission loss (STL) [1], while structural cores are investigated towards their high stiffness to mass ratio [2]. More recently, research is done towards the vibro-acoustic performance of sandwich panels with structural cores such that they consider all three conflicting requirements [3]. In [4], the STL of sandwich panels with corrugated cores is investigated, while in [5] sandwich panel cores are presented combining all three requirements. Several works, e.g. [6–9], have investigated the influence of the core topology of the sandwich panel on the vibro-acoustic performance. Often periodicity is used while designing these sandwich structures, i.e. a certain supercell which consists of a partition of sheet and core is repeated in the plate direction [10].

To design these structures which comply with the different conflicting requirements, optimization techniques are important enablers. The optimization of sandwich panels to their vibro-acoustic performance has been studied by many researchers and can be categorized in three groups: (i) parameter optimization which optimizes the thickness and material of the homogeneous core and face sheets [11], (ii) size optimization which optimizes the geometrical parameters of corrugated, honeycomb or truss cores, e.g. [12–15] and (iii) topology optimization in which the core can converge to any topology, e.g. [5, 16–18]. From the optimized sandwich structures, mostly designs resulting from parameter or size optimization are experimentally validated on 3D panels, e.g. [12], while experimental validation of topology optimized sandwich panels is scarce. Only recently, Wang et al. [19] experimentally validated a topology optimized core. However, while their optimization is done in 2D, it was necessary to execute the experiment with a 3D panel resulting in effects during the experiment not considered in the optimization. Therefore, this work focuses on the direct experimental validation of designs coming out of 2D optimization frameworks. This enables a fast and early validation of novel sandwich core designs and verification of the underlying exploited phenomena, avoiding the need to execute 3D optimization, simulations or manufacturing. More specifically, the focus is put on the experimental validation of topology optimized 2D sandwich structures since the topology optimization gives the user the most design freedom. The framework of Cool et al. [5] is of interest since it recently obtained novel sandwich cores which comply with the three conflicting requirements of being light-weight, having a good stiffness and obtaining a high STL in the targeted frequency ranges. Additionally, the physical phenomena to achieve the high STL, namely a *mode-conversion* effect, is not yet experimentally proven.

Note that also in other fields of application, the experimental validation of topology optimized structures is limited and has only raised attention in recent years. Several 2D optimized structures are experimentally validated, e.g. concrete beams to their static stiffness [20], buckling tests are done on functionally graded lattices [21] and magnetic active structures [22]. Also the experimental validation of optimized thermal [23] and water wave [24] cloaking designs is shown recently. In [25], acoustic topology optimized metasurfaces are tested for reflective wavefront modulation. The 2D optimized structures are experimentally validated on a *near-2D* structure which exists of the 2D design while this is extended with a limited thickness in the third direction.

Regarding the experimental validation of the STL of finite structures, denoted the *finite STL* further on, a quick and easy set-up to validate optimized 2D structures is

lacking. Current techniques for measuring the STL can be generally divided into on the one hand methods originating from building acoustics, which consider larger (single or double panel) plates and diffuse field acoustic excitations, and on the other hand methods derived to investigate smaller samples under normal or specific oblique incidence.

In the first category, three groups of techniques can be specified: (i) Firstly, the most widely used set-up to measure the STL of a panel-like structure is the two-room method [26, 27]. The investigated plate is mounted between an anechoic and reverberant room. By placing a source in the reverberant chamber and microphones in both chambers, the STL can be computed [12]. (ii) Secondly, the STL can be determined using a sound intensity measurement while the panel is mounted at one or between two closed rooms [27]. In this case, the panel is excited by an acoustic source at one side and the desired output surface is scanned with a sound intensity probe to determine the STL [27]. The disadvantage of above mentioned techniques is that the panel needs to be mounted such that no transmission occurs via the flanking paths. (iii) Thirdly, to overcome the limitations of difficult mounting requirements, techniques exploiting correlation and the Fourier-transform have been proposed [28, 29]. These techniques have the advantage that the panel does not have to be mounted between two separate rooms since the different transmission paths can be detected. However, the difference in energy between the different transmission paths needs to be large enough.

In the second category, again three groups of methods have been developed: (i) Firstly, for 1D normal plane wave propagation, transmission tube measurements can be used [30]. This method considers a small sample to characterize the STL of the entire structure. The method has several disadvantages. It is limited to normal acoustic excitations, it is not straightforward to install the sample in the set-up and to control its boundary conditions, which can have a major impact on the results. Additionally, because of the small sample size, the modal behavior of the panel is not considered during the analysis. (ii) Secondly, several Fourier-based techniques exist to perform reflection and transmission measurements in waveguides. In [31], it is proposed to use microphones at the input and output side of the sample together with a modal decomposition and Fourier-Lommel transform to experimentally determine the reflection and transmission. (iii) Finally, Zhang et. al [32] recently proposed a method to determine the absorption and transmission coefficient of materials using the modal decomposition method in a rectangular waveguide. This technique can enable the computation of the characteristic STL of the material. The last two techniques fail, however, at the cut-on frequencies of the waveguide.

Although various techniques exist to experimentally determine the STL, almost all methods are proposed for 3D panels. Moreover, the experimental set-ups require an acoustic excitation and/or an acoustic output measurement. The described techniques above are, therefore, cumbersome to adapt to the validation of near-2D structures since a 2D acoustic wave field is practically hard to achieve, acoustic leakage in the third direction is difficult to avoid, etc. This shows the need for an experimental set-up to verify the STL of near-2D structures enabling a fast and early validation of novel proposed (optimized) sandwich core designs.

This work focuses on the experimental validation of the 2D finite STL of novel (optimized) vibro-acoustic sandwich panels. Firstly, a methodology is presented to experimentally determine the 2D finite STL with an effective, yet simple, purely structural set-up using a near-2D sample. Secondly, with the proposed methodology, the sandwich core

designs resulting from a previously proposed vibro-acoustic topology optimization framework [5] are experimentally validated. More specifically, the exploited mode-conversion effect to achieve high STL in the targeted frequency range is experimentally shown. After numerically investigating the optimized design in terms of performance and robustness towards the geometry and material properties, the structure is fabricated, measured and compared to two reference cases consisting of the equivalent mass and double mass beam case. With the executed experiments, the effectiveness of the proposed experimental validation is shown and the mode-conversion effect, specifically observed in the investigated sandwich structure, is experimentally proven.

The rest of this paper is structured as follows. Sec. 2 gives an overview of the problem under investigation. Sec. 3 elaborates on the applied topology optimization on the supercell level with the infinite STL as objective and discusses its results. In Sec. 4 the STL of the finite structure is investigated, as will be present in reality. Finally in Sec. 5, a methodology is proposed to experimentally determine the 2D finite STL after which the experimental validation is described and discussed. Conclusions are given in Sec. 6.

2. Problem description

A 2D finite sandwich panel is envisaged consisting of two structural plates with a vibro-acoustic core in between which is a repetition of a number of supercells (n_{sc}), schematically visualized in Fig. 1a. The sandwich panel is surrounded at the top and bottom by two-dimensional infinite acoustic half spaces consisting of the same fluid (density $\rho_a = 1.225$ kg/m^3 and speed of sound $c_a = 340$ m/s). The structure is excited by an incident plane acoustic pressure wave at the bottom with amplitude P_i and acoustic wave number $k_a = \omega/c_a$, with ω (rad/s) the radial frequency. This results in a transmitted wave at the top with amplitude P_t and reflected wave at the bottom with amplitude P_r. The three zeroth order acoustic waves are given in the frequency domain by:

$$p_i(x,y) = P_i \mathrm{e}^{\mathrm{i}(-k_x x - k_y y)}, \quad p_t(x,y) = P_t \mathrm{e}^{\mathrm{i}(-k_x x - k_y y)}, \quad p_r(x,y) = P_r \mathrm{e}^{\mathrm{i}(-k_x x + k_y y)}, \tag{1}$$

in which $k_x = k_a sin(\theta)$, $k_y = k_a cos(\theta)$ represent the trace wavenumbers, θ is the angle of incidence and the term $\mathrm{e}^{\mathrm{i}\omega t}$ is excluded for convenience. Note that for non-homogeneous structures, higher order acoustic harmonics are present as well. In this work, only the first harmonic is considered which is valid under the assumptions that the structure is weakly periodic and subwavelength [33]. The performance indicator of interest is the STL which is defined by the ratio of the transmitted to incident pressure amplitude [1]:

$$\mathrm{STL}(\omega,\theta) = -10\log_{10}\left(\tau(\omega,\theta)\right), \qquad \tau(\omega,\theta) = \left|\frac{P_t}{P_i}\right|^2, \tag{2}$$

in which τ is denoted by the sound power transmission coefficient.

In a first step, the sandwich panel will be optimized using the topology optimization framework of [5]. The optimization is executed on the supercell level (see Fig. 1b) while assuming infinite periodicity in the x-direction. This choice is made since it leads to a decreased computational cost for the optimization. The supercell has a dimension of

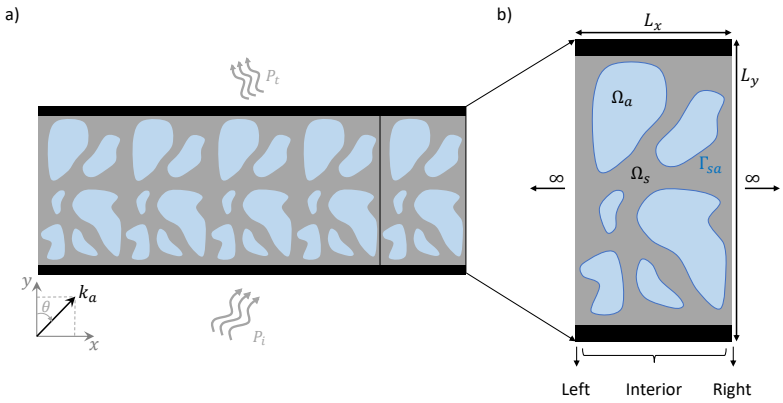

Figure 1: Schematic overview of problem under investigation. a) Finite 2D sandwich panel consisting of five supercells. b) Supercell representing the corresponding infinite periodic sandwich structure.

$L_x \times L_y$ and is discretized with the finite elements (FE) technique using bilinear square plane strain elements for the structural domain (Ω_s), while using linear elements for the acoustic domain (Ω_a). The mesh consists of a rectangular grid with $N_x \times N_y$ elements. Assuming time-harmonic motion, this results in the following system of equations [1]:

$$\left(-\omega^2 \underbrace{\begin{bmatrix} \mathbf{M}_s & 0 \\ \mathbf{S}_u & \mathbf{M}_a \end{bmatrix}}_{\mathbf{M}} + \underbrace{\begin{bmatrix} \mathbf{K}_s & \mathbf{S}_p \\ 0 & \mathbf{K}_a \end{bmatrix}}_{\mathbf{K}} \right) \underbrace{\begin{bmatrix} \mathbf{u} \\ \mathbf{p} \end{bmatrix}}_{\mathbf{q}} = \underbrace{\begin{bmatrix} \mathbf{f}_s \\ \mathbf{f}_a \end{bmatrix}}_{\mathbf{f}} + \underbrace{\begin{bmatrix} \mathbf{e}_s \\ \mathbf{e}_a \end{bmatrix}}_{\mathbf{e}}, \tag{3}$$

in which the subscripts s, a denote the structural and acoustic domain, respectively. $\mathbf{M}, \mathbf{K}, \mathbf{S}$ represent the mass, stiffness and coupling matrices. Each node consists of three degrees-of-freedom (DOFs), being the x- and y-displacement, denoted as the vector $\mathbf{u}$ over all nodes, and the pressure, denoted as the vector $\mathbf{p}$ over all nodes. $\mathbf{q}, \mathbf{f}, \mathbf{e}$ represent, respectively, all DOFs of the supercell, the internal forces and external forces. The infinite periodicity is mathematically applied using the Bloch-Floquet boundary conditions [34]. Using a periodicity matrix $\mathbf{\Lambda}$, the nodal DOFs are related to the periodic DOFs vector $\hat{\mathbf{q}}$ which only contains the left and interior DOFs (cf. Fig. 1b) using the constant $\lambda_x = e^{-\mathrm{i}\mu_x}$ with $\mu_x = k_x L_x$. This results in a modified system of equations:

$$(\hat{\mathbf{K}} - \omega^2 \hat{\mathbf{M}})\hat{\mathbf{q}} = \hat{\mathbf{e}}, \qquad \hat{\mathbf{K}} = \mathbf{\Lambda}^H \mathbf{K} \mathbf{\Lambda}, \qquad \hat{\mathbf{M}} = \mathbf{\Lambda}^H \mathbf{M} \mathbf{\Lambda}, \qquad \hat{\mathbf{e}} = \mathbf{\Lambda}^H \mathbf{e}, \tag{4}$$

see [35] for details. Using this equation, the infinite STL corresponding to the supercell structure can be computed using the WFE technique [5, 33]. For this, the surrounding acoustic halfspaces are modeled using an analytical formulation, while continuity conditions are applied to translate the structural displacement into the required pressure information. The reader is referred to [5] for a more detailed description of the infinite STL calculation.

The specific case under investigation in this work consists of a supercell with dimensions 50×55 mm, while the thickness of the plates is considered equal to 2.5 mm. The FE

have a size of 0.417 mm such that the mesh is sufficiently accurate for both the acoustic and solid waves in the frequency range considered. The material for the structural part is polymethyl methacrylate (PMMA), from which the material properties are taken over from [36], i.e. a Young's modulus $E = 4.85(1 + 0.05\mathrm{i})$ GPa in which the complex part represent the structural damping, a density $\rho_s = 1188.35$ kg/m^3, and Poisson's ratio $\nu = 0.31$. The fluid characteristics in the core are equal to the surrounding fluid, while a small ratio of acoustic damping is included in the core by using a complex speed of sound: $\rho_a = 1.225$ kg/m^3 and $c_a = 340(1 + 2 \cdot 10^{-4}\mathrm{i})$ m/s.

3. Topology optimization

In this work, the supercell core, representing the infinite sandwich panel, is optimized using the topology optimization framework of [5]. The applied topology optimization framework is presented in detail in [5] and here only used to obtain an optimized sandwich structure design for the specific case under investigation. This section gives first a brief overview of the applied framework, after which the results are discussed for the case of the specific geometrical and material properties as given before. The section ends with an investigation towards the robustness of the optimized design.

3.1. Optimization framework overview

The core of the sandwich panel is optimized using a gradient-based density topology optimization framework [5]. The supercell is discretized with a structured FE mesh, while each element is controlled with a design variable $\boldsymbol{\xi}$ which ranges from 0, representing fluid, to 1, representing solid. A total of N_e variable are considered in the optimization. The vibro-acoustic coupling in the core is considered during the optimization using the method by Jensen [37]. As usual in topology optimization, the design variable field ($\boldsymbol{\xi}$) will be projected onto the required physical density field $\boldsymbol{\xi}_P$ which determines the stiffness and mass matrices to execute the FE analysis and obtain the desired objective and constraints. In this work, a robust formulation [38] is used, meaning that in each iteration, three designs are investigated: an eroded (e), blueprint (b) and dilated (d) design. This leads to a minmax problem in which the worst case of the three designs drives the optimization. See Appendix A for details on the conversion from $\boldsymbol{\xi}$ to $\boldsymbol{\xi}_P$, the robust formulation and the construction of the system matrices. The distribution of material ($\boldsymbol{\xi}$) will be optimized during the optimization to maximize the STL in the frequency range of interest. Two constraints are as well added to the optimization: (i) a constraint on the volume usage ($v_{d,P}$) in the design domain and (ii) a constraint on the static compliance (θ_{st}) when a distributed force is added at the top side and the bottom side is constrained. The second constraint is added to ensure that the top and bottom panel remain connected [5]. The optimization problem which is solved reads as follows:

$$\begin{cases} \min\limits_{\boldsymbol{\xi}\in\mathbb{R}^{N_e}} & \max(-\mathrm{STL}_e(\Delta\omega,\theta), -\mathrm{STL}_b(\Delta\omega,\theta), -\mathrm{STL}_d(\Delta\omega,\theta)) \\ \text{s.t.} & v_{d,\mathrm{P}}/V - 1 \leq 0 \\ & \theta_{\mathrm{st}}/\mu_{\mathrm{st}}\hat{\theta}_{\mathrm{st}} - 1 \leq 0 \\ & 0 \leq \boldsymbol{\xi} \leq 1, \end{cases} \tag{5}$$

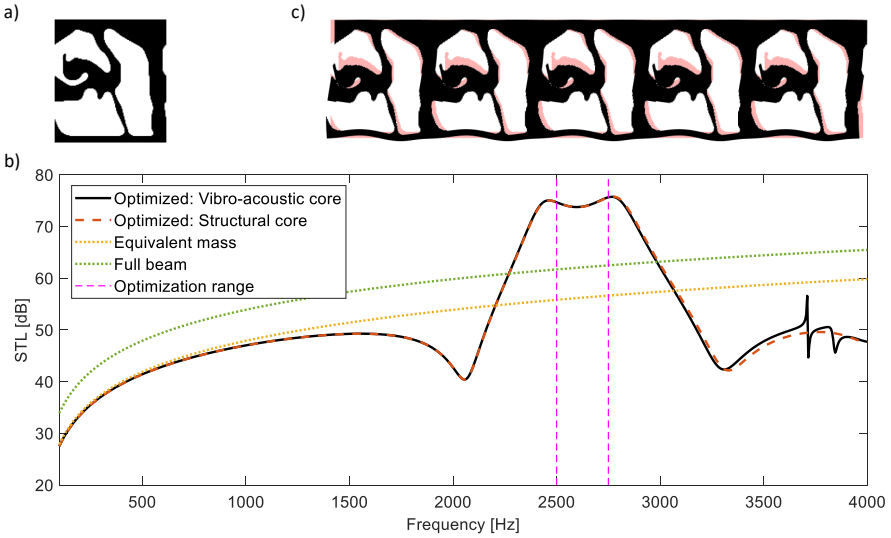

Figure 2: Result of the topology optimization framework. a) The optimized blueprint design. b) The corresponding infinite STL considering both with and without air in the core. Plotted together with the equivalent mass and full beam design. c) The vibration displacement of the optimized design at 2625 Hz.

in which $\Delta\omega$ represent the frequency range of interest, $\mathrm{STL}(\Delta\omega, \theta)$ is the combined STL over the frequency range of interest determined with a numerical integration technique, V is the maximum allowed volume fraction, $\hat{\theta}_{\mathrm{st}}$ is the static compliance of a full solid design (all design variables equal to 1) and μ_{st} determines the maximum allowable static compliance. Elaborate details on the construction of the optimization problem can be found in [5].

With the geometrical and discretization choices of previous section, 14400 design variables are considered during the optimization. The other framework choices are as follows: $V = 0.5$ representing 50% material usage with respect to a full solid beam with the same dimensions, $\theta_{\mathrm{st}} = 10$, $\theta = 0^o$ representing normal incidence and $\Delta\omega$ lays between 2500 Hz and 2750 Hz in which 12 equidistant evaluations are considered during the optimization. The other optimization specific parameters are taken over from [5]. Note that during the discussion of the results in the rest of this manuscript, a broader frequency range is plotted, ranging from 100 Hz till 4000 Hz.

3.2. Result

Running the optimization framework with the specific geometrical, material and optimization parameters as stated before, the blueprint design of Fig. 2a is obtained. It consists of a straight connection between the top and bottom panel, a second more sloped, slender connection and a curved horizontal connection between the two. The infinite STL of this design is computed while on the one hand considering the vibro-acoustic core and on the other hand while only modeling the structural part and neglecting the acoustic part in the core (Fig. 2b). On top of that, the infinite STL of the equivalent mass

case (solid design with supercell dimensions 50×27.5 mm) and the double mass case, denoted as the full beam case (solid design with supercell dimensions 50×55 mm) are plotted. From this, two observations can be made. (i) The optimized design shows a high STL in the frequency range of optimization. It outperforms both the equivalent mass case and full beam case by 17.59 dB and 11.73 dB (at 2625 Hz), respectively. Note that the full beam case has twice the mass of the optimized case. (ii) As shown in [5, 39], it is required to consider the acoustic parts in the core during the topology optimization, since otherwise the acoustic path can have a non-negligible impact during the post-processing of the designs. Therefore, a vibro-acoustic optimization is performed in this work. In this particular final optimized design, it is the structural transmission path in the core which is the path of least resistance, cf. Fig. 2b. Only at higher frequencies (> 3500 Hz), two acoustic resonances (3710 Hz and 3845 Hz) are perceived. Since this is outside the frequency range which is optimized, the post-processing of this structure can be done on a purely structural core, neglecting the acoustic part in the core. For this reason, the acoustic part is not considered in the rest of this manuscript. Note that this comes with the limitation that the proposed methodology is only valid for structures in which the structural part of the sandwich core is the dominant transmission path [39].

The high STL is enabled due to two principles [5]. (i) The mass-spring-mass frequency of the design occurs before the frequency range of optimization, leading to a *mode-cancelling* principle in the sandwich panel [40]. (ii) Also a *mode-conversion* occurs, as can be seen in the vibration amplitude plot in Fig. 2c. The mode conversion enables the conversion of the bending in the bottom panel to a mainly in-plane compression motion of the top panel. These effects can also be perceived in the 1D structural dispersion curves of the supercell. The dispersion curves are obtained by computing the eigenvalues of Eq. (4) [35]. In this work, the inverse approach is used in which the propagation constant λ_x is imposed and the system is solved towards the frequency ω. The resulting dispersion curves and four wave modes are visualized in Fig. 3. Starting from zero, a bending mode (i) and compression mode (ii) occur, visualized in Fig. 3b. At 2065 Hz, the second bending mode cuts-on, a typical phenomenon at the decoupling of a double panel [1]. This cut-on results in a dip in the corresponding STL (cf. Fig. 2b). Next, it is seen that in the frequency range where the STL peak occurs, a mode veering is present in the dispersion curves [41]. The mode veering shows there is a coupling between the compression and bending mode. This can also be seen in the wave mode plots in Fig. 3b.

3.3. Robustness

In the literature, the influence of various parameters, i.e. geometrical and material properties, on the vibro-acoustic performance of sandwich panels has been studied for various sandwich core designs, e.g. [6, 42, 43] and references therein. In this section, the robustness of the STL performance of the optimized design of previous section is investigated since this work aims to execute an experimental validation in which several uncertainties are present. First of all, manufacturing tolerances exist, therefore Sec. 3.3.1 investigates the robustness of the STL performance towards changes in the geometry. Secondly, the material properties may deviate from the ones used in the optimization, therefore Sec. 3.3.2 briefly investigates the robustness towards changes in the material.

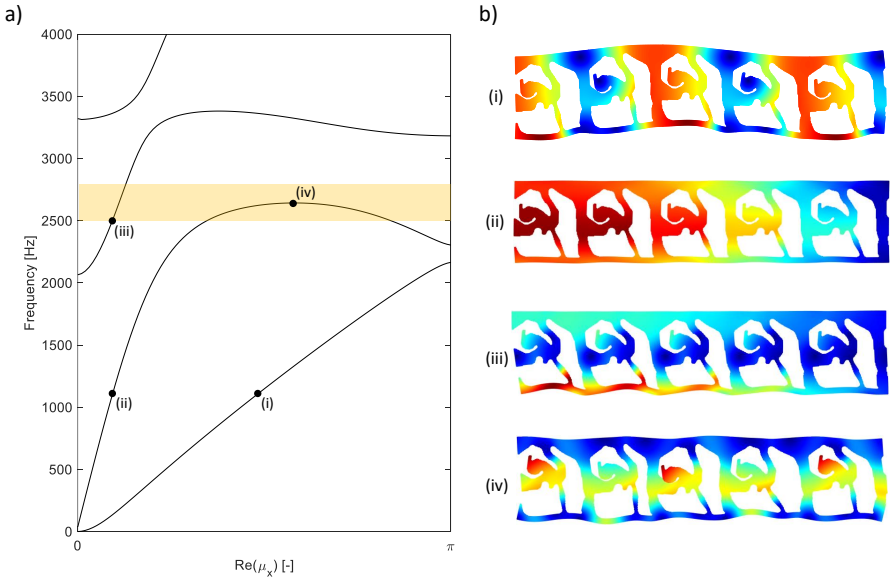

Figure 3: Structural dispersion curve results of the optimized design. a) 1D dispersion curve with in yellow the frequency band that is optimized. b) Visualization of four modes (using five supercells) of the dispersion curves. The coloring indicates the magnitude of the displacement with red being largest and blue lowest.

3.3.1. Robustness towards geometry

In the optimization framework, a robust formulation using an eroded, blueprint and dilated design is applied, mainly for regularization purposes [5, 38]. However, due to this formulation, also a performance robustness towards the geometry, or in other words manufacturing tolerances, is embedded. Fig. 4a shows the eroded, blueprint and dilated design next to each other. It can be seen that the three designs represent the same topology while the eroded is more slender than the blueprint design and the dilated is thicker than the blueprint design. The difference between eroded-blueprint and blueprint-dilated is between one and two discretization elements, resulting in an absolute difference of $0.4 - 0.8$ mm at the boundaries of the geometry. Note that the number of element difference between the three designs can be tuned by changing the specific filtering properties of the double filtering technique [5, 44].

Fig. 4b shows the corresponding STL performance of the eroded, blueprint and dilated design. A number of observations can be made. Firstly, it is seen that the STL performance in the optimized frequency range is high for all three designs. This entails that if due to manufacturing tolerances, the design is more eroded or dilated with respect to the blueprint design, still an excellent performance will be obtained in the envisaged frequency range. Secondly, the STL curves all have a similar course, only with a shift in frequency. The eroded design is shifted to lower frequencies, while the dilated design is shifted to higher frequencies. This can be understood because the eroded design will have a slightly smaller mass and stiffness, while the dilated design has a slightly higher

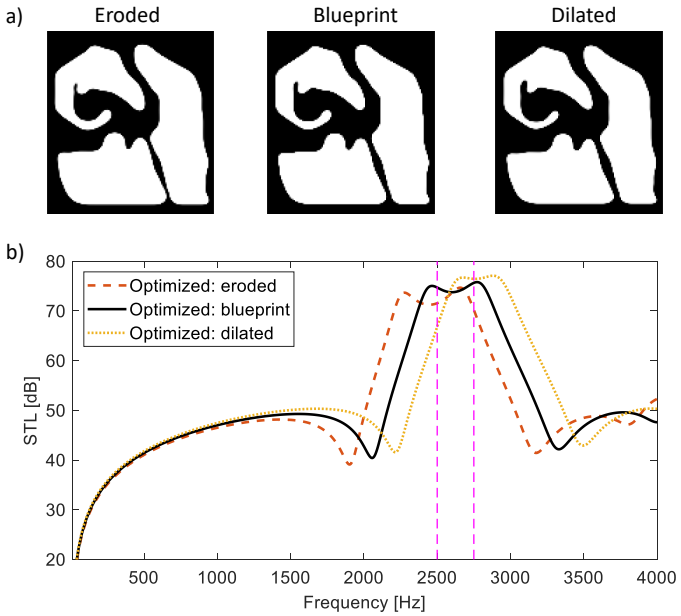

Figure 4: Investigation of robustness to STL performance towards manufacturing tolerances. a) The eroded, blueprint and dilated design resulting from the optimization. b) The corresponding STL performance.

mass and stiffness with respect to the blueprint design. Overall, it can be concluded that the optimized design is robust towards small changes in the geometry.

3.3.2. Robustness towards material properties

In view of a physical realization, it is of interest to investigate the performance of the design with respect to perturbations of the material properties since another batch of the material can show changes in the properties. The infinite STL of the optimized blueprint design is each time computed while one of the material properties (Young's modulus, density, Poisson's ratio and structural damping) is changed with an increase or decrease of 10%.

The results are shown in Fig. 5. Firstly, it can be seen that with the possible perturbations, in all cases a high STL performance is achieved in the frequency range of interest. However, due to the changes, a frequency shift of the STL peak is observed and the highest STL changes slightly. More specifically, it can be said that the structural damping and Poisson's ratio have a negligible effect with respect to a change in the Young's modulus and density. As expected from standard structural dynamics and due to the modal behavior in the optimized frequency range, a change in structural damping will only lead to a small shift in frequency, while mainly a shift (0.42 dB) is obtained in STL level. A decrease in Poisson's ratio will lead to a shift of 30 Hz towards lower frequencies while the level does not change. A similar trend is seen for a change in the Young's modulus while bigger shifts occur, namely a decrease in Young's modulus

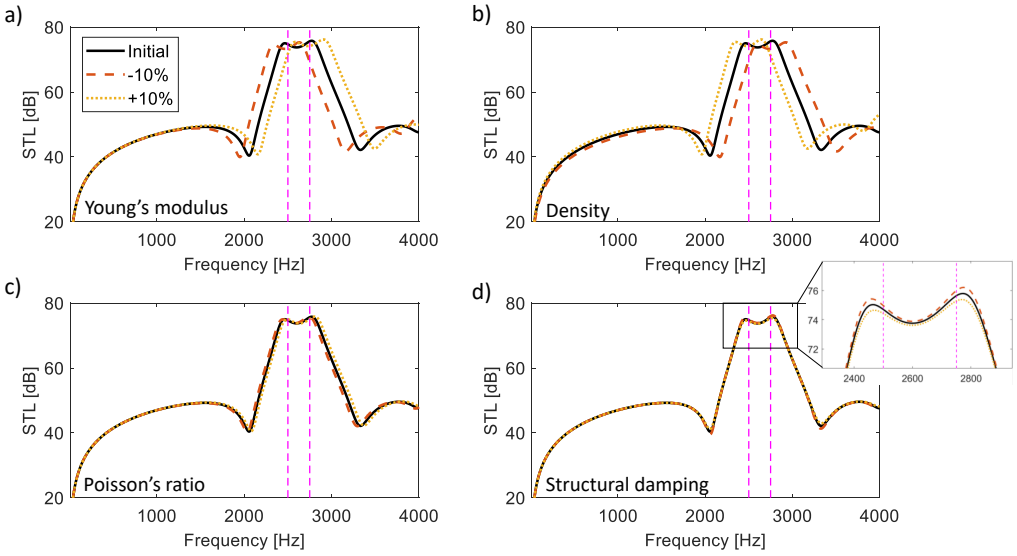

Figure 5: Investigation of robustness to STL performance towards several material uncertainties: a) Young's modulus, b) density, c) Poisson's ratio, d) structural damping.

leads to a shift of 140 Hz to lower frequencies while the maximum STL level lowers with 0.42 dB. An increase leads to a shift to higher frequencies with 125 Hz while the level increases with 0.42 dB. The shift in frequencies is to be expected since a lower Young's modulus leads to a less stiff design resulting in a shift to lower frequencies of the decoupling frequency (as observed in the STL curve). The behavior of the density perturbation is the opposite to the Young's modulus. Now a 10% decrease leads to a shift of 125 Hz in higher frequencies and a lowering of the maximum STL level with 0.42 dB. This change in behavior is explainable since a decrease of mass leads generally to a higher frequency content. Overall, it can be concluded from this study that the optimized design is robust towards possible perturbations in the material properties.

4. Finite STL

Now that the optimized design is obtained on the supercell level, this section investigates the STL when considering a finite number of supercells. In Sec. 4.1, the applied methodology to compute the finite STL is given after which the STL is investigated with an increasing number of optimized supercells in Sec. 4.2.

4.1. Methodology

Fig. 6a shows the problem overview to compute the finite STL. A finite beam is excited at the bottom by a plane wave, after which the sound radiated by the beam is determined using the Rayleigh integral [1]. Specifically, the radiated sound is computed by integrating over a half-circle at a distance R_R which is large enough to represent the far field ($k_a R_R \gg 1$). The problem is translated to the numerical problem visualized in Fig. 6b in which the

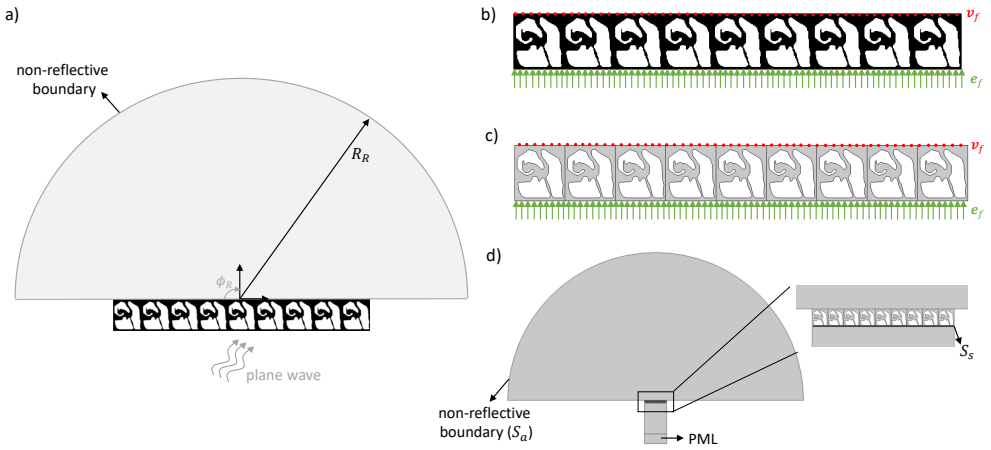

Figure 6: Finite STL calculation. a) Problem description. b) Numerical model and design in Matlab. c) Numerical model and design in Comsol. d) Comsol verification with acoustic excitation and output.

acoustic halfspaces are, as before, modeled using an analytical formulation. Next to the Rayleigh integral, other techniques exist to compute the finite STL while not explicitly evaluating the acoustic halfspaces [45]: (i) the equivalent radiated power in which the fluid's characteristic impedance is used, (ii) the elementary radiator approach [46] and (iii) an approximation based on the volume velocity [47].

Using the Rayleigh integral, at the input side ($y = 0$), the incident power on the finite structure can be easily computed since the sound intensity of the incident plane wave equals $|p_i|^2 / 2\rho_a c_a$ and is parallel to the propagating wave [48]:

$$W_i(\omega) = \frac{L_x n_{sc} |p_i|^2 cos(\theta)}{2\rho_a c_a}. \tag{6}$$

Next, the acoustic plane wave excitation is translated into equivalent nodal forces on the (flat) interface of the structure. By assuming the back-coupling (from structure to acoustics) is negligible, the system is excited by a blocked pressure wave with amplitude $2P_i$ [49, 50]. The consistent external nodal forces are lumped on the transverse DOFs j at the bottom of the structure as:

$$e_f^j(x_j) = 2P_i \alpha_j \mathrm{e}^{-\mathrm{i}(k_x x_j)} \qquad j \in [1 \dots N_f^b], \tag{7}$$

in which N_f^b is the number of transverse DOFs at the bottom and α_j represent the relation between the distributed pressure and the nodal force and can be computed using the element shape functions. For a rectangular regular interface mesh, α_j is the same for all nodes and equals L_x/N_x, except on the boundaries where it is $L_x/2N_x$. This external excitation is now used to solve the system of equations of the finite part, which is given by:

$$\left(\mathbf{K}_f - \omega^2 \mathbf{M}_f\right) \mathbf{u}_f = \mathbf{e}_f, \tag{8}$$

with $\mathbf{K}_f, \mathbf{M}_f$ the structural stiffness and mass matrices of the finite part and $\mathbf{u}_f$ the displacement DOFs. Note that this could also be a vibro-acoustic system when including the acoustic parts in the core of the sandwich panel. As discussed before, the acoustic part in the core is negligible for the particular design under investigation.

At the output side ($y = L_y$), the transmitted power will be determined using the Rayleigh integral [1, 12]. After solving Eq. (8), the sound pressure in the far field radiated from the beam can be determined from the vibrations of the top surface of the beam [1]. More specifically, the transmitted pressure at a radius R_R is computed by integrating over the top surface of the beam x_t as:

$$p_t(R_R, \phi_R, \omega) = \frac{\rho_a \omega}{2} \int_0^{n_{sc} L_x} \mathbf{v}_f H_0^2(k_a |\mathbf{r} - \mathbf{r}_t|) dx_t \approx \frac{\rho_a \omega}{2} \Delta x_t \sum_{m=1}^{n_t} \mathbf{v}_f^m H_0^2(k_a |\mathbf{r} - \mathbf{r}_t^m|) \quad (9)$$

in which H_0^2 is the Hankel function of zeroth order and second kind, $\mathbf{v}_f = \mathrm{i}\omega \mathbf{u}_f$ is the transverse surface velocity, $\mathbf{r}_t = (x_t, L_y)$ represents the coordinate on the top of the beam and $\mathbf{r} = (x_r, y_r)$ represents the coordinate on the half-circle and is fully determined by R_R and ϕ_R. Note that practically, this integral is approximated by a numerical integration scheme in which n_t represent the number of considered output observation points, Δx_t the distance between consecutive points and the superscript m indicates the evaluation of the variable at point m. Next, the time-averaged acoustic intensity of the transmitted wave can be computed as:

$$I_t(R_R, \phi_R, \omega) = \frac{1}{2} \Re \left(p_t(R_R, \phi_R, \omega) v_r^H(R_R, \phi_R, \omega) \right) \approx \frac{1}{2\rho_a c_a} \left| p_t(R_R, \phi_R, \omega) \right|^2, \quad (10)$$

in which v_r^H is the complex conjugate of the radial component of the fluid particle velocity and is approximated in the far field by $v_r^H = p_t^H / \rho_a c_a$. Finally, the total acoustic radiated power by the beam is obtained by integrating the average acoustic intensity over the half-circle in the far field:

$$W_t(R_R, \omega) = \int_0^{\pi} I_t(R_R, \phi_R) R_R d\phi_R, \quad (11)$$

similar as before, a numerical integration technique is used to approximate this continuous integral. Finally, the STL of the finite structure can be computed by the ratio of the transmitted to incident power, $\tau = W_t / W_i$ and filling this into Eq. (2).

4.2. Result and discussion

First of all, the implementation and validity of the 2D Rayleigh integral is verified with the commercial software Comsol Multiphysics after which the STL of the finite structure is investigated with an increasing number of supercells n_{sc}. A finite case with $n_{sc} = 9$ is selected for the verification while the supercell is slightly shifted to have a closed left and right edge (as shown in Fig. 6b). Note that for the verification, the number of n_{sc} may be chosen randomly. As a first verification, the optimized design obtained in Matlab is smoothened and loaded into Comsol. With this structure, the Matlab implementation is imitated (Fig. 6c) by performing a purely structural analysis with a force input as given in Eq. (7). After the calculation, the corresponding velocities at the top side are extracted from Comsol and used in Eqs.(9-11) to compute the corresponding STL. As

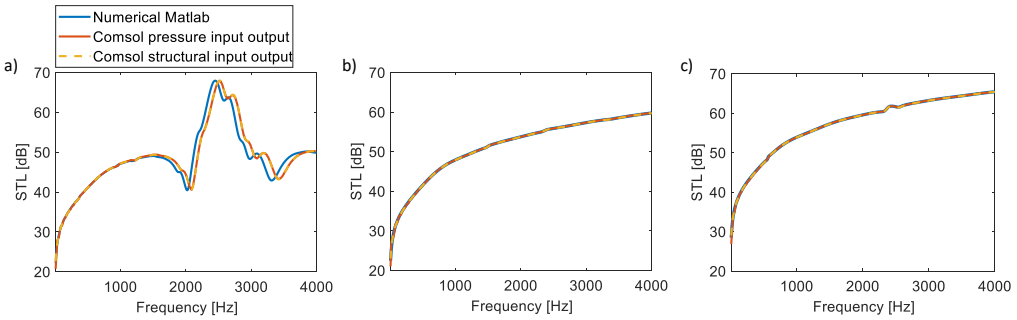

Figure 7: Verification of the Matlab implementation for a finite case with 9 supercells using the commercial software Comsol Multiphysics with an acoustic/structural input/output for a) the optimized structure, b) the equivalent mass case and c) the full plate.

a second verification, the STL is computed entirely in Comsol using an acoustic input and acoustic output. The schematic of the numerical model is visualized in Fig. 6d. The finite structure has an acoustic space at the bottom under which a perfectly matched layer (PML) is modeled to remove any reflections. The top acoustic halfspace is also entirely modeled with acoustic elements and a non-reflective boundary condition is applied in terms of an impedance boundary to limit the computational cost. Next, the STL is computed by integrating over the output pressure (p_o) at the non-reflective boundary S_a and the background pressure (p_b) at the input side S_s:

$$STL_{Comsol} = 10 \log_{10} \left(\frac{\int_{S_a} |p_o| \, dS_a}{\int_{S_s} |p_b| \, dS_s} \right). \tag{12}$$

The results for the optimized design, equivalent mass case and full beam case are shown in Fig. 7. It can be seen that for the equivalent mass case and the full beam case a perfect match is achieved. For the optimized design, both Comsol simulations are corresponding indicating that the STL computation using a purely structural simulation is a good approximation of the acoustic excitation and output. The STL achieved with Matlab corresponds also very well with the Comsol verification, the slight shift in frequency is due to (i) the smoothening of the design from the structured design representation in Matlab to the body-fitted design representation in Comsol and (ii) the deletion of the remaining intermediate design variables, denoted gray-values, in the topology optimization to the full black and white design in Comsol.

Now that the methodology is verified, the finite STL is investigated for an increasing number of supercells (n_{sc}). The number of supercells is increased starting from three up until a repetition of 60 supercells, leading to a finite part with a length of 0.15 m to 3 m, respectively. The resulting finite STL is plotted in Fig. 8 together with the corresponding infinite STL of the optimized structure, the equivalent mass case and full beam case. First of all, what can be seen, is that even with only three supercells, the optimized design outperforms the infinite full beam case in the targeted frequency range. Next, it is seen that with an increase of n_{sc}, the STL performance increases towards the infinite STL. Asymptotically, for n_{sc} going to infinite, the infinite STL performance will be obtained

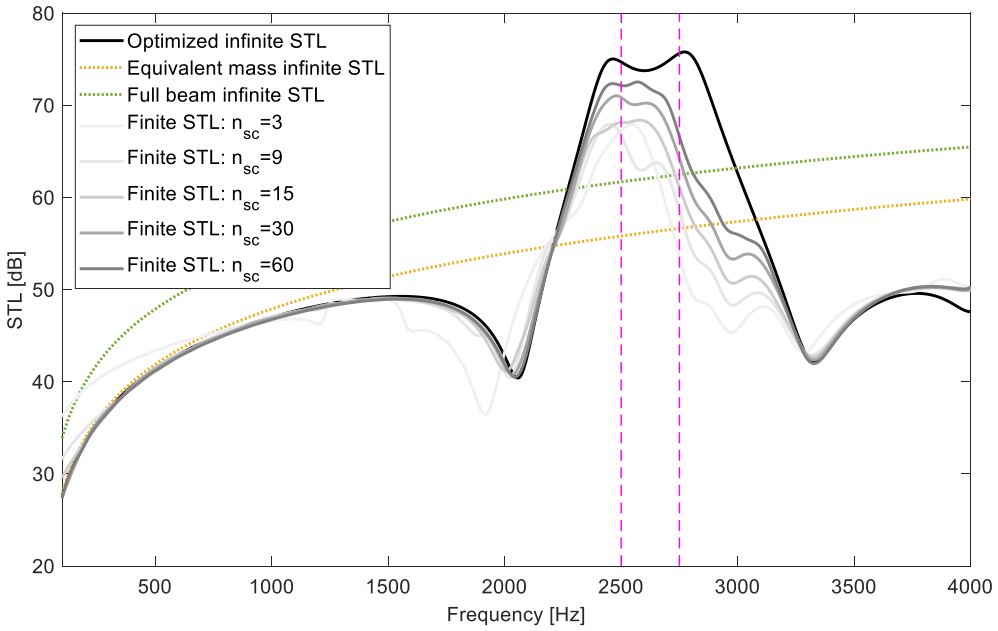

Figure 8: Investigation of the finite STL with an increasing number of supercells and free boundary conditions at the left and right boundary. The infinite STL for the optimized design, equivalent mass case and full mass case are plotted as a reference.

again. The decrease in STL performance when going to a finite structure was expected and is explained due to two effects. (i) Firstly, in the finite structure, edge effects will be present at the left and right edge of the structure. Sangiuliano et al. [51] discussed the effect of finiteness to a locally resonant metamaterial beam. It was concluded that due to the edge effects, resonant modes of the finite structure could appear in the bandgap leading to a decrease of the performance. Although this particular design does not rely on a bandgap, a similar phenomenon will occur in which sound radiation can appear at the edges of the beam which is not present in the infinite counterpart. (ii) Secondly, the optimized structure plays upon the assumption of infinite periodicity by exploiting a veering effect between the bending and translational mode (cf. Sec. 3.2). The smaller the finite counterpart, the less this can be exploited by the finite modes leading to a decreased STL performance. Finally, note that here the left and right edge of the finite part have free boundary conditions. The finite STL will change when fixed or sliding boundary conditions are applied. More specifically, a stiffening of the finite structure will lead to a shift to higher frequencies of the STL peak and a decrease in maximum achieved STL. Since the aim of this work is to experimentally validate the optimized STL effect, it is opted to work with free boundary conditions. Moreover, the n_{sc} is chosen equal to nine as a trade-off between the STL performance and dimensions of the finite sample.

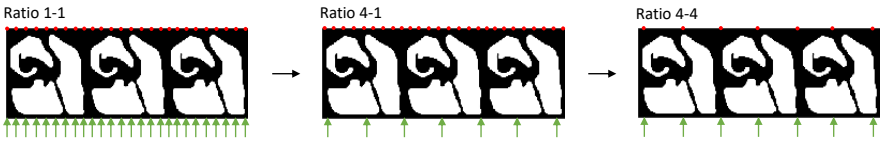

Figure 9: Reasoning to experimentally determine the 2D STL with a purely structural input and output. From left to right, first the input is approximated with a coarser discretization. Next, the velocity at the top is integrated using a coarser sampling.

5. Experimental validation

This section gives an overview of the experimental validation. Firstly, a methodology is presented to experimentally determine the 2D finite STL in Sec. 5.1, after which the set-up is discussed in Sec. 5.2. Next, a discussion of the results is given in Sec. 5.3.

5.1. Experimental STL calculation based on vibration measurements

In Sec. 4.1 it is shown numerically that the 2D STL can be determined using a purely structural excitation and structural output. For this, the plane wave excitation is lumped to the transverse DOFs at the bottom of the structure, while the transmitted pressure is computed using the transverse velocity DOFs at the top. Following this reasoning, the 2D STL could experimentally be determined if all frequency response functions (FRFs) between the input excitation and output observation points are known. However, to make this practically feasible in an experimental setting, the number of input and output points needs to be decreased, as demonstrated in Fig. 9. More specifically, the input plane wave will be lumped at a small number of excitation points at the bottom of the structure, while the output velocity will only be analyzed using again a coarse number of observation points. The influence of coarsening the grid of observation points has been briefly discussed in previous works for 3D plates, e.g. [46, 52]. In this section, the focus is on the influence of coarsening both the grid of excitation and of observation points to approximate the STL of 2D finite structures.

At the input side ($y = 0$), the plane wave excitation can be lumped at the bottom of the beam at less DOFs than present in the FE discretization, cf. Fig. 9 step one. More specifically, if a ratio R^b is used, the plane wave excitation is translated to a structural input force at N_f^b/R^b equidistant transverse DOFs at the bottom with an amplitude given as:

$$e_f^j(x_j) = R^b 2 P_i \alpha_j \mathrm{e}^{-\mathrm{i}(k_x x_j)} \qquad j \in [1 \dots N_f^b/R^b]. \tag{13}$$

Note that (i) the total input force is the same due to the scaling, (ii) this reasoning can be followed for normal and oblique incident plane waves.

Next, at the output side, the transmitted pressure is computed out of a numerical integration of the transverse velocity (cf. Eq. (9)). The number of used observation points n_t can again be coarsened, using a ratio factor of R^t (see Fig. 9 step two). This leads to the following adaptation of the numerical integration scheme:

$$p_t(R_R, \phi_R, \omega) \approx \frac{\rho_a \omega}{2} R^t \Delta x_t \sum_{m=1}^{n_t/R^t} \mathbf{v}_f^m H_0^2(k_a |\mathbf{r} - \mathbf{r}_t^m|). \tag{14}$$

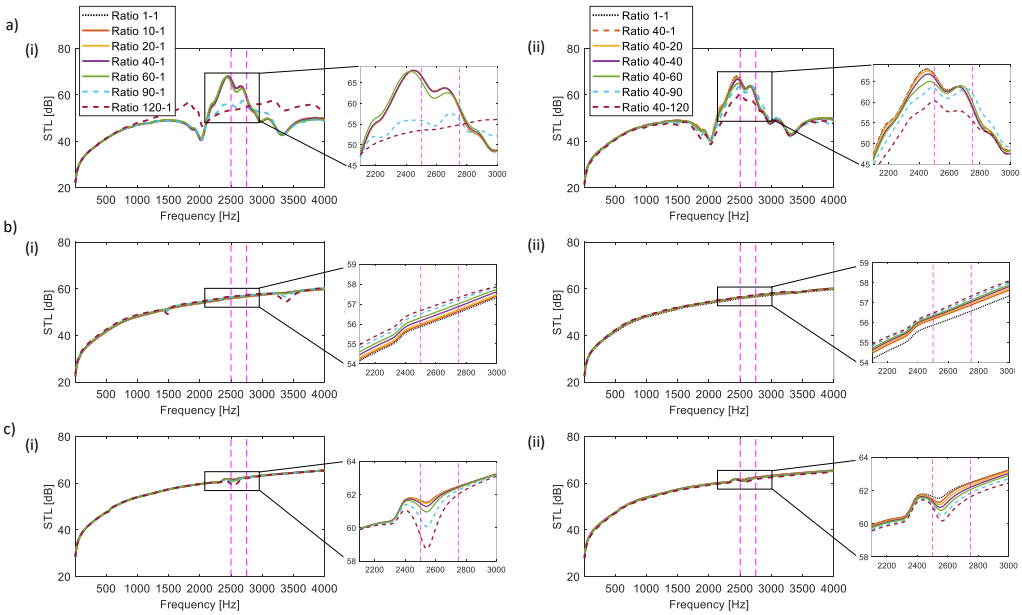

Figure 10: Verification of the approximate STL calculation on a) the optimized structure, b) the equivalent mass and c) the full beam. i) Investigation of the required bottom ratio with a zoom shown in the subplots. ii) Investigation of the required top ratio.

The accuracy of the rectangle rule for numerical integration depends on the accuracy of the piecewise constant approximation of the velocity at the top panel. The same holds for the discretization of the continuous pressure load on the bottom panel. In both cases, the required number of sampling points depends on the wavelength of the relevant wave types, similar to the well-known six elements per wavelength rule-of-thumb in dynamic FE analyses. Hence, the choice for the ratio R^b and R^t will be dependent on the dynamics present in the system and is investigated for the optimized design, equivalent mass case and full beam case. For convenience, the notation *Ratio* R^b-R^t is used in what follows, while *Ratio* 1-1 denotes no extra coarsening of the bottom and top occurs.

First the result of the optimized design is discussed. In Fig. 10a.i, the influence of increasing R^b is shown, with a zoombox at the optimized frequency range. Overall, a good estimate of the STL can be obtained till a ratio of $R^b = 60$, meaning the input pressure wave is discretized with only 19 discrete nodal forces. It is observed (by comparing e.g. the ratio of $R^b = 40$ and $R^b = 60$) that the STL slightly drops in the optimized frequency range with an increase of R^b while shifting the peak to the lower frequencies. For higher R^b values, larger discrepancies are visible. An $R^b = 40$ is used in this work since it ensures that the difference due to the coarsening of the input results in a STL difference of less than 1 dB. Note that an $R^b = 40$ means that the plane acoustic wave is approximated by 28 distinct point force excitations. Next, in Fig. 10a.ii, the influence of the choice of R^t is further investigated with the choice of $R^b = 40$. The approximation of the STL drops with an increase of R^t, as expected, since an increase of R^t leads to a coarser

approximation of the velocity field at the top. Overall, however, it can be said that the coarsening of the top part has a smaller influence than the coarsening of the bottom part. Again, to limit the change in STL to 1 dB, an R^t of 40 is selected for this optimized design.

In Fig. 10b and Fig. 10c, the references cases are investigated for an increase in R^b and R^t. The conclusions are very similar to the optimized design. Overall, an almost exact estimate of the STL is obtained with the largest investigated R^b-value of 120, meaning the input is approximated with 10 discrete nodal forces. In the equivalent mass case it is seen that a coarsening of the input and output leads to an increase in the STL. For the high R^b-values, small discrepancies start to occur at 1495 Hz and 3385 Hz. These are corresponding to the second and third bending eigenfrequency of the finite structure. For a uniform excitation, these are non-efficient radiation modes since a zero net displacement occurs. However, due to the coarse discretization of the excitation, these eigenfrequencies are not uniformly excited anymore along the structure leading to a non-negligible effect in the STL. In the full beam case, a small anti-resonance is present in the frequency range that was optimized. Here the increase of R^b and R^t leads to a decrease of the frequency in that region. As for the optimized case, the increase of R^b has more influence than an increase of R^t. Overall, even for the largest R^b and R^t values investigated, namely a ratio of 120, an approximation of the STL with an error smaller than 2 dB is obtained. In this work, a bottom and top ratio of 40 is selected for both reference cases to be consistent with the optimized case.

Now that the ratios are known, the experiment can be conducted. Practically, this goes as follows. Each input point will be structurally excited separately with a point load. For the choice of $R^b = 40$, this means 28 excitation points. For each of these excitation points, the normal velocity at the determined output points will be measured. With the choice of $R^t = 40$, this results in a measurement at 28 output points. More specifically, the FRF between all input and output points is experimentally measured after which these are combined by (i) scaling it with the right excitation force (cf. Eq. (13)), (ii) multiplying it with the thickness in the z-direction of the third dimension, (iii) summing all resulting velocity outputs at each observation point for all excitation points. The third step is possible by the linearity of the system:

$$\mathbf{e}_f = \sum_m \mathbf{e}_f^m, \qquad \mathbf{u}_f = \sum_m \mathbf{u}_f^m, \qquad \left(\mathbf{K_f} - \omega^2 \mathbf{M_f}\right) \mathbf{u}_f^m = \mathbf{e}_f^m. \tag{15}$$

Note that if a nonlinear system would be under investigation, the excitations cannot be done separately while the output measurements can still be done with a roving accelerometer technique. This, however, will make the technique cumbersome to execute.

Before proceeding to the execution of the measurements and after running the topology optimization, a numerical procedure has to be followed. (i) Firstly, it needs to be checked that the structural path in the core is the dominant path. (ii) Next, the amount of supercells should be chosen to represent the finite part, cf. Fig. 8. (iii) Finally, the ratios R^b and R^t need to be selected with a numerical analysis as discussed in this section.

Property	Initial	Updated	% change	Updating method
Density $[kg/m^3]$	1188.35	1177.16	-0.94	Weighing
Young's modulus [GPa]	4.85	4.83	-0.457	Modal updating
Poisson's ratio [-]	0.31	0.345	+11.3	Modal updating
Structural damping [-]	0.05	0.0466	-6.8	Half power bandwidth

Table 1: Results of the updating of the PMMA properties.

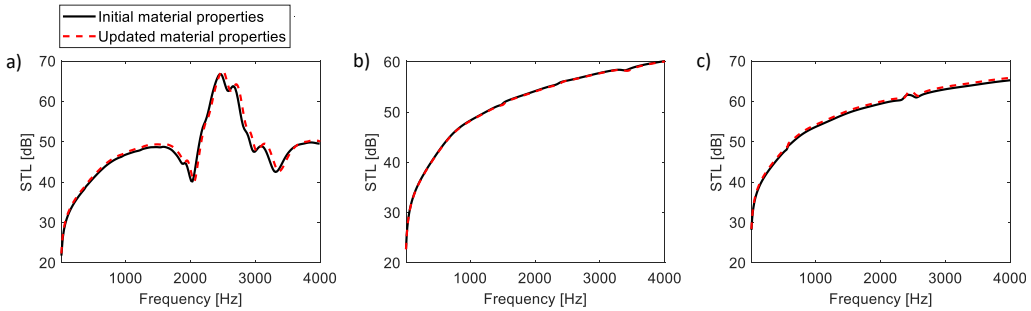

Figure 11: Finite STL result with a ratio of 40-40 for the a) optimized design, b) equivalent mass and c) full beam. Each design is computed with the initial and updated material properties, as given in Tab. 1.

5.2. Set-up

Before executing the experiment, the PMMA parameters are updated by weighting and performing a modal updating of a PMMA panel with dimensions $120 \times 180 \times 8$ mm. Note that a thickness of 8 mm is selected to minimize the amount of out-of-plane modes in the samples under investigation. The modal updating is performed in Siemens NX while considering the frequencies and modeshapes of the first six free-free modes. The numerical model used for the updating consists of a shell CQUAD4 mesh with a size of 5 mm. After the updating, the average mismatch between the numerical model and the measurements is 0.401%. The modal damping is estimated by the half power bandwidth method. Tab. 1 gives an overview of the initial and updated material parameters and the percentage change. It is seen that mainly the Poisson's ratio and structural damping coefficient are changed, while the density and Young's modulus have a change smaller than 1%. Fig. 11 shows the finite STL of the three designs computed with the initial and updated material properties. As expected from Sec. 3.3, the change in material properties only has a small influence on the performance. In the rest of the manuscript, the updated material properties are applied in the shown numerical simulations.

Next, the experimental set-up is discussed as shown in Fig. 12a. The tested samples are visualized in Fig. 12b together with the corresponding dimensions and the weight of the samples. The samples are manufacturing using a laser cutting process. Note that for the optimized design, the dilated design is used during the laser cutting process since the laser will erode the structure. By selecting the dilated design, the manufactured design will lay close to the blueprint design. The sample under investigation is freely hinged at

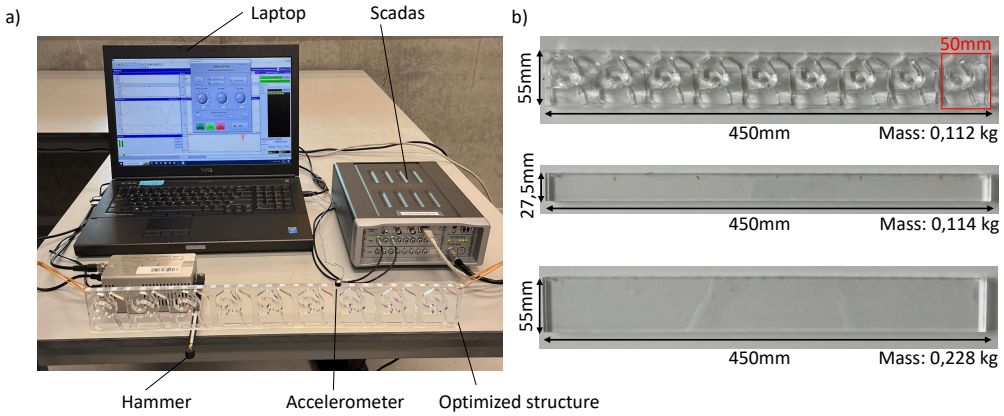

Figure 12: Overview of the experiment. a) The experimental set-up with the optimized design suspended. b) The optimized design sample, equivalent mass sample and full plate sample with corresponding dimensions.

the top left ($x = 0, y = L_y$) and top right ($x = L_x n_{sc}, y = L_y$) corners, this was done by making two holes of 1.5 mm in diameter in the structures which were made at 3 mm and 6 mm from the edges. The force input is given at the bottom of the structure with an automatic hammer of the type NV Tech SAM 1. The automatic hammer is preferred above a shaker due to the lightweight character of the structures. The hammer is always positioned such that the excitation occurs perpendicular to the bottom of the structure and on the middle line. For the response measurements, a 1D lightweight accelerometer (type PCB35A24 with a weight of 0.8 g) is attached to the top of the structure. A laser vibrometer is not suitable due to the hinged free-free construction. For the data acquisition a *Simcenter Scadas Mobile* device is used in combination with the *Siemens LMS Test.Lab version 2021.2* software for the signal processing. During the experiment a combined roving hammer and roving accelerometer strategy is applied such that all bottom points are excited and all resulting top points are measured. More specifically, each input point is excited separately and as many times as there are output points because for each excitation point, the acceleration is measured at the different output points in a consecutive fashion.

5.3. Results and discussion

This section provides a discussion of the results. Firstly, Sec. 5.3.1 discusses the results of both references cases, after which the results of the optimized design are given in Sec. 5.3.2.

5.3.1. Equivalent mass and full beam

Fig. 13a shows the numerically obtained (with ratio $40 - 40$) and measured STL for the equivalent mass case and the full beam case. The summed velocities $\mathbf{v}_f$ at all 28 output points due to excitation at all 28 input points can be found in Appendix B, Figs. B.16,B.17. An excellent match is seen between the numerical and measured results, validating the proposed methodology and set-up. Some artifacts can be observed

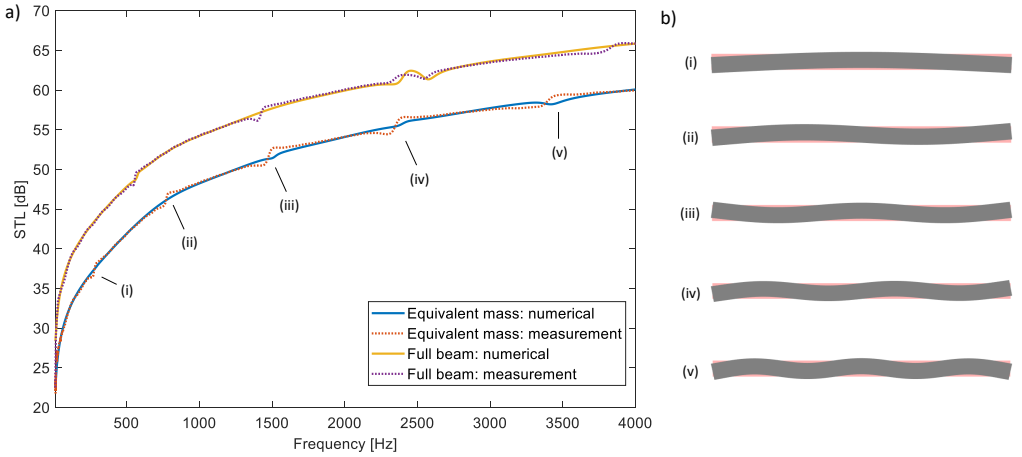

Figure 13: Results of the experiment for the equivalent mass case and full beam case. a) The numerical STL with ratio $40-40$ and the experimental result. b) Five bending modes obtained with Matlab at (i) 293 Hz, (ii) 788 Hz, (iii) 1495 Hz, (iv) 2372 Hz and (v) 3384 Hz. The red shows the beam without displacement, while the black visualizes the beam with displacement.

in the equivalent mass cases, indicated with (i)-(v) in Fig. 13a. These spurious peak-dip appear around the frequencies where the 2D free bending eigenmodes can be found in the numerical model Fig. 13b. In the numerical model, the contribution of the large eigenmodes displacement is not seen in the STL since an overall zero-displacement takes place. However, due to small measurement errors and noise in the experiment, the zero-net displacement is approximately zero leading to a small dip-peak behavior. For the full beam case, similar observations can be made. A good STL approximation is obtained and small dip-peak behaviors are seen in the experimental result around the bending eigenmodes of the plate, which will now occur at higher frequencies with respect to the equivalent mass case.

5.3.2. Optimized design

In this section, the results of the experiment on the optimized design are discussed. The obtained velocity measurements at each output point are given in Appendix B. From the velocity plots, it can be seen that the velocity outputs contain much more dynamics than in the references cases. However, still a good match between the numerical computations and the measurements is obtained. Also note that the velocity outputs have a minimum which is an order of magnitude smaller than the minimum of the reference cases. Using these velocity outputs, the resulting STL is shown in Fig. 14a together with the numerically obtained result. For convenience, the results of the equivalent mass and full beam are repeated here. A good match is perceived between the experimental data and the numerical data. The results show that the optimized design obtains a higher experimental STL than the two reference cases in the optimized frequency range. The optimized design outperforms the equivalent mass case with an average of 8 dB and peak of 11 dB in the targeted frequency range, while it outperforms the full beam case with an average of 3 dB and maximum of 6 dB. Note that since only information in the targeted

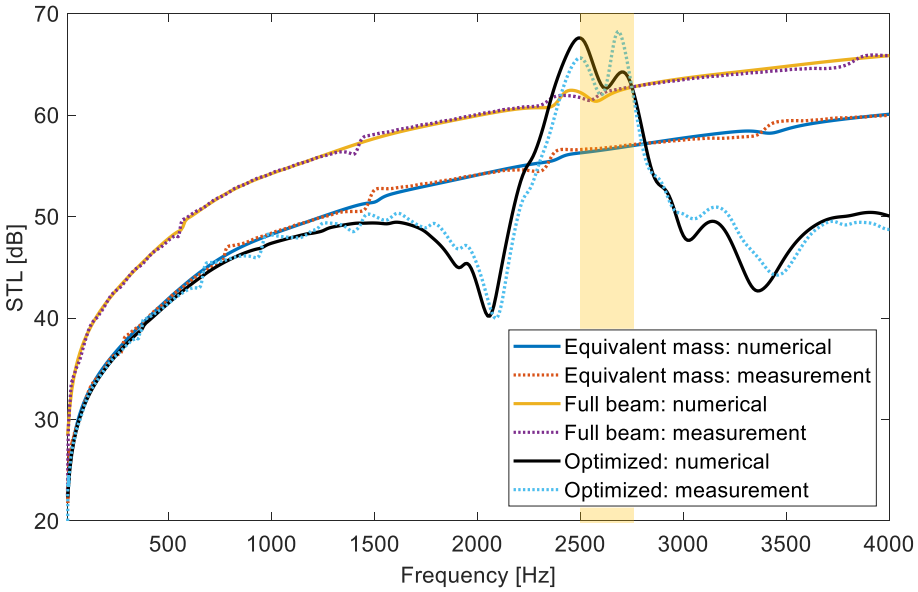

Figure 14: Results of the experiment for the optimized design. The numerical STL with ratio $40-40$ and the experimental result (together with the references cases). The yellow band indicates the numerically optimized frequency range.

frequency range of $2500-2750$ Hz is provided to the optimizer, it cannot be expected that the optimized design outperforms the reference cases outside of this region. A ripple is observed in the experimentally obtained STL. This can be understood similarly to the spurious peak-dip behaviors in the previous section. Due to the complexity of the structure, many bending modes are present in the structure. However, still a very good match is obtained with the 2D numerical data.

Next, it is investigated what happens if not the entire length is excited, i.e. not all 28 points are considered during the STL computation. This study is possible due to the specific construction of the experiment. The STL is computed when only points $1-7$, $1-14$, $1-21$ or all input points are excited (see results in Fig. 15). Physically, this can be interpreted as if only 1/4, 1/2, 3/4 or the entire length of the beam is excited by a plane wave. From this study, the following insights are obtained: (i) the measurement and numerical simulation correspond well for the different cases, making this an interesting test to verify the experiment, (ii) the optimized effect is fully exploited when the entire beam is excited, or with other words, the combination of all output velocities enable a cancellation effect leading to the high STL.

Overall, it can be concluded that the numerically optimized effect is clearly visible in the experiment and optimized beam outperforms both references cases on average with more than 8 dB and 3 dB, respectively, for the equivalent mass case and full beam case in the targeted frequency range.

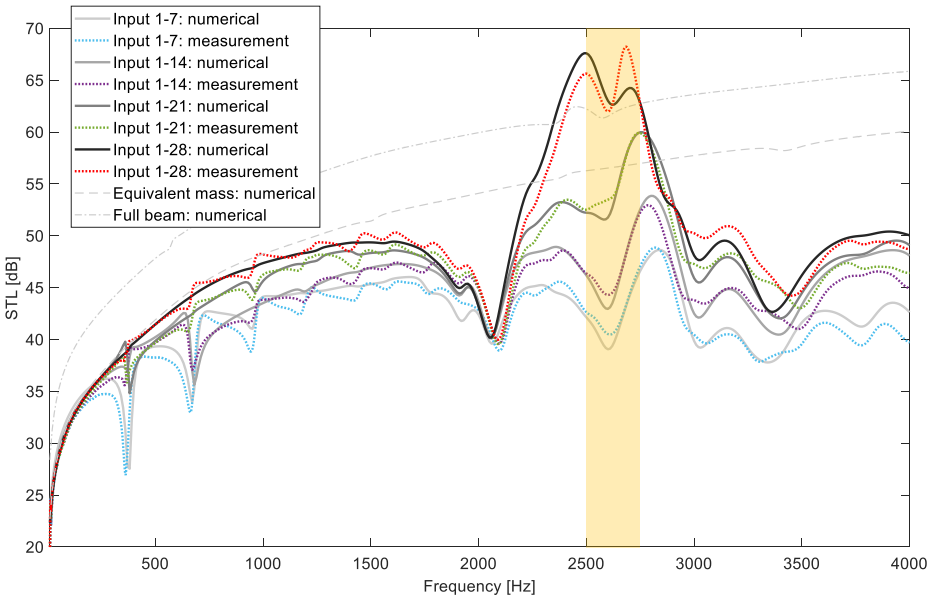

Figure 15: Numerical and measured STL result for an increasing amount of considered excitation points. Plotted together with both reference cases. The yellow band indicated the numerically optimized frequency range.

6. Conclusion

This work proposes an experimental validation for the 2D finite STL of sandwich panels. In a first step, a supercell is optimized which represent an infinite periodic sandwich beam. This is done with a gradient-based vibro-acoustic topology optimization framework using the robust formulation. In post-processing, it is shown that the optimized design achieves a high STL in the optimized frequency range and outperforms both the equivalent mass case and full beam case which has a double mass. The high STL is achieved by both a mode-cancelling and mode-conversion effect. Also the robustness of the optimized design in terms of the geometry (or manufacturing tolerances) and material properties is investigated showing a shift in frequency can occur while the optimized effect remains visible. Next, the finite STL is investigated using the 2D Rayleigh integral. When going from infinite to finite, a decrease in achieved STL is perceived, mainly due to edge effects. However, already with three supercells, the design outperforms both reference cases numerically. The more supercells are considered, the closer the performance reaches the infinite one.

In view of executing an experimental validation, a methodology is presented to calculate the 2D STL with a purely structural experiment, i.e. by means of structural excitations and response measurements on a limited set of excitation and measurements points. This is possible by exploiting the linearity of the system. Next, the optimized design, the equivalent mass and the full beam case (with twice the mass as the optimized design) are fabricated and tested. The experimental results show a good match with the numerical simulation, proving the optimized design outperforms both reference cases with an

average of 8 dB and 3 dB, respectively, in the optimized frequency range. Furthermore, the numerically perceived optimized effects, i.e. the employed mode-conversion effect of the particular investigated sandwich design, are experimentally validated. Small artifacts are present in the experimental results which are explained by the bending modes.

In conclusion, a fast experimental validation technique is proposed with which 2D sandwich designs can be experimentally validated showing the structure's potential for achieving extraordinary acoustic insulation in various applications.

Acknowledgments

The research of V. Cool (fellowship no. 11G4421N) is funded by a grant from the Research Foundation - Flanders (FWO). The Research Fund KU Leuven is gratefully acknowledged for its support.

Appendix A. Topology optimization framework

This appendix gives further information regarding the optimization framework. A complete description can be found in [5].

Appendix A.1. From design variables to physical density fields

The topology optimization uses the variables $\boldsymbol{\xi}$ internally as design variables. The physical density fields, representing the design, are obtained using a sequence of density filters and Heaviside projections. More specifically, a robust formulation is used which employs an eroded (e), blueprint (b) and dilated (d) design [38] while these are obtained with the double filtering technique of [44]. The density filtering [53] is defined as follows:

$$\tilde{\xi}^e = \frac{\sum_{i=1}^{N_e} w(\xi^e - \xi^i)\xi^i}{\sum_{i=1}^{N_e} w(\xi^e - \xi^i)}, \qquad w(\xi^e - \xi^i) = \max\left(0, R - ||\xi^e - \xi^i||_2\right), \tag{A.1}$$

and represents an averaging of the element design variables over a certain radius R. The Heaviside projection [54] is used to push the variables towards black and white (1 and 0) values and is given by:

$$\bar{\xi}^e = \frac{\tanh(\eta\beta) + \tanh((\xi^e - \eta)\beta)}{\tanh(\eta\beta) + \tanh((1-\eta)\beta)}, \tag{A.2}$$

in which η is the projection level and β is the projection strength. The physical density fields are now obtained using the following operations:

$$\boldsymbol{\xi} \xrightarrow[R_1]{\text{Eq. } (A.1)} \tilde{\boldsymbol{\xi}} \xrightarrow[\eta_1,\beta_1]{\text{Eq. } (A.2)} \bar{\tilde{\boldsymbol{\xi}}} \xrightarrow[R_2]{\text{Eq. } (A.1)} \bar{\bar{\tilde{\boldsymbol{\xi}}}} \xrightarrow[(\eta_e,\eta_b,\eta_d),\beta_2]{\text{Eq. } (A.2)} (\bar{\bar{\tilde{\boldsymbol{\xi}}}}_e, \bar{\bar{\tilde{\boldsymbol{\xi}}}}_b, \bar{\bar{\tilde{\boldsymbol{\xi}}}}_d) = (\boldsymbol{\xi}_{e,\mathrm{P}}, \boldsymbol{\xi}_{b,\mathrm{P}}, \boldsymbol{\xi}_{d,\mathrm{P}}), \tag{A.3}$$

with $(\eta_e, \eta_b, \eta_d) = (\eta_b + \Delta\eta, \eta_b, \eta_b - \Delta\eta)$. The result after the operations are the physical eroded, blueprint and dilated design fields.

Appendix A.2. Obtaining the system matrices

Having the physical design fields, the material characteristics per element (Young's modulus E^e, density ρ_s^e, bulk modulus of the fluid κ^e and density of the fluid ρ_a^e) are obtained with selected interpolation technique. In this work, the RAMP interpolation method is employed [55] together with a linear interpolation to obtain the material properties per element:

$$\begin{cases} E^e(\xi_{\mathrm{P}}^e) = E_v + \frac{\xi_{\mathrm{P}}^e}{1+q(1-\xi_{\mathrm{P}}^e)}(E - E_v), \\ \rho_s^e(\xi_{\mathrm{P}}^e) = \rho_v + \xi_{\mathrm{P}}^e(\rho_s - \rho_v), \\ \frac{1}{\kappa^e(\xi_{\mathrm{P}}^e)} = \frac{1}{\kappa} + \xi_{\mathrm{P}}^e(\frac{1}{\kappa_r} - \frac{1}{\kappa}), \\ \frac{1}{\rho_a^e(\xi_{\mathrm{P}}^e)} = \frac{1}{\rho_a} + \frac{\xi_{\mathrm{P}}^e}{1+q(1-\xi_{\mathrm{P}}^e)}(\frac{1}{\rho_r} - \frac{1}{\rho_a}), \end{cases} \tag{A.4}$$

in which E_v, ρ_v, κ_r and ρ_r are artificial material properties to avoid numerical problems in the optimization. Using these material properties, the mass, stiffness and coupling matrices of Eq. (3) are obtained by summing over all element contributions:

$$\begin{aligned} \mathbf{K}_s &= \sum_{e=1}^{N_e} E^e(x,y)\mathbf{K}_s^e, & \mathbf{M}_s &= \sum_{e=1}^{N_e} \rho_s^e(x,y)\mathbf{M}_s^e, \\ \mathbf{K}_a &= \sum_{e=1}^{N_e} \frac{1}{\rho_a^e(x,y)}\mathbf{K}_a^e, & \mathbf{M}_a &= \sum_{e=1}^{N_e} \frac{1}{\kappa^e(x,y)}\mathbf{M}_a^e, \\ \mathbf{S}_p &= \sum_{e=1}^{N_e} (1-\xi_{\mathrm{P}}^e)\mathbf{S}^e, & \mathbf{S}_u &= \sum_{e=1}^{N_e} \xi_{\mathrm{P}}^e(\mathbf{S}^e)^T. \end{aligned} \tag{A.5}$$

Note that the vibro-acoustic coupling in the core is considered during the optimization using the method by Jensen [37]. Now that the system matrices are known, the objective and constraints can be computed.

Appendix A.3. Optimization problem

Due to the robust formulation, a minmax optimization problem is obtained, cf. Eq. (5). This is rewritten towards a bounded formulation:

$$\begin{cases} \min\limits_{\boldsymbol{\xi}\in\mathbb{R}^{N_e}, z} \quad z \\ \text{s.t.} \quad -\dfrac{\mathrm{STL}_e(\Delta\omega,\theta)}{C} + 1 - z \le 0 \\ \quad\quad -\dfrac{\mathrm{STL}_b(\Delta\omega,\theta)}{C} + 1 - z \le 0 \\ \quad\quad -\dfrac{\mathrm{STL}_d(\Delta\omega,\theta)}{C} + 1 - z \le 0 \\ \quad\quad\quad v_{d,\mathrm{P}}/V - 1 \le 0 \\ \quad\quad\quad \theta_{\mathrm{st}}/\mu_{\mathrm{st}}\hat{\theta}_{\mathrm{st}} - 1 \le 0 \\ \quad\quad\quad z \ge 0, \quad 0 \le \boldsymbol{\xi} \le 1, \end{cases} \tag{A.6}$$

in which C represents a scaling factor to have a normalization of the constraints, chosen as 200 in this work. Note that the volume constraint is computed on the dilated design while the static stiffness constraint is evaluated for the eroded design. This optimization problem is solved using the Method of Moving Asymptotes [56].

Appendix B. Velocity plots

Figs. B.16-B.18 show the measured and numerically obtained velocity at each output point summed over all input points for the equivalent mass, full beam and optimized case, respectively.

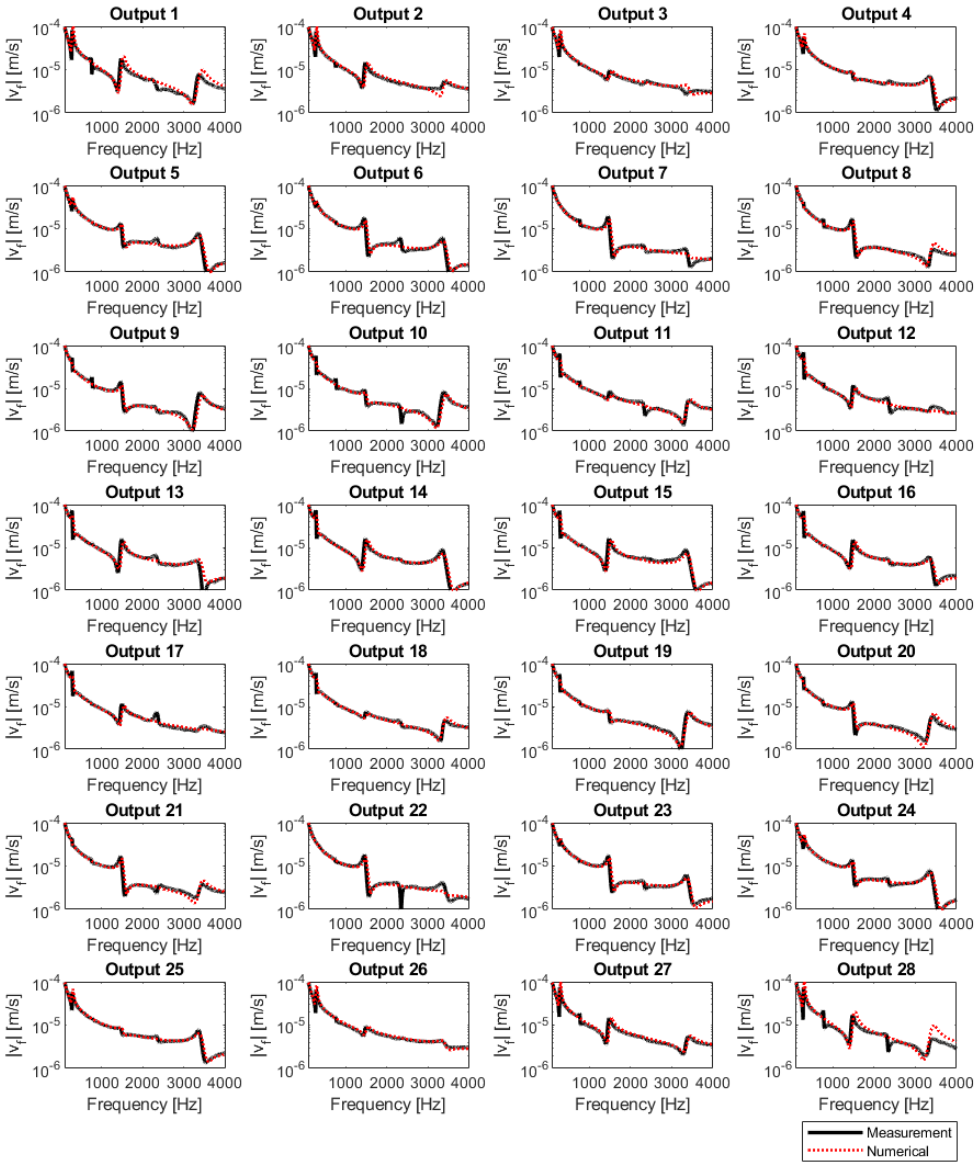

Figure B.16: Numerical and measured velocity at every output point for the equivalent mass, obtained by summing up all velocities at that point over the different excitation points.

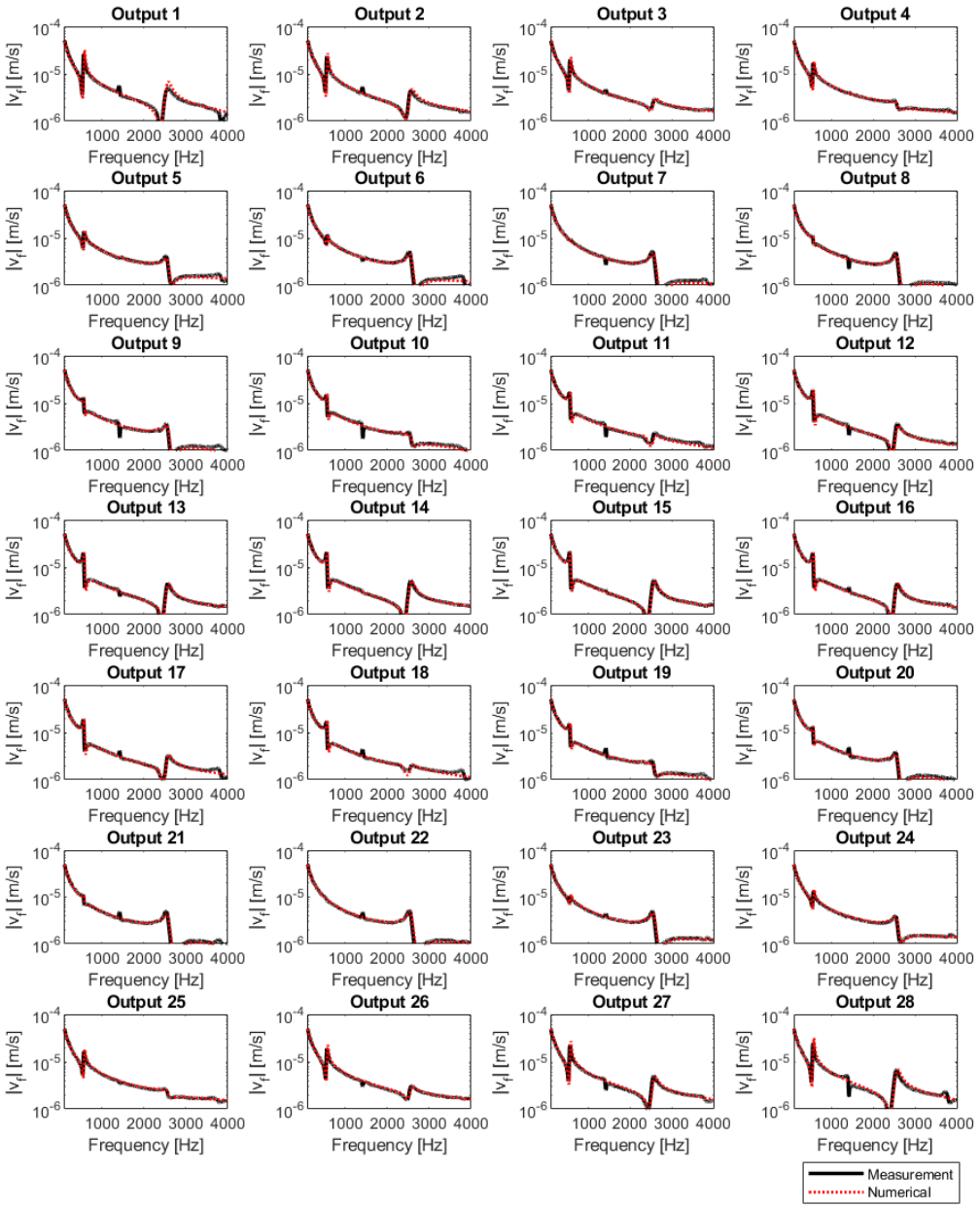

Figure B.17: Numerical and measured velocity at every output point for the full beam, obtained by summing up all velocities at that point over the different excitation points.

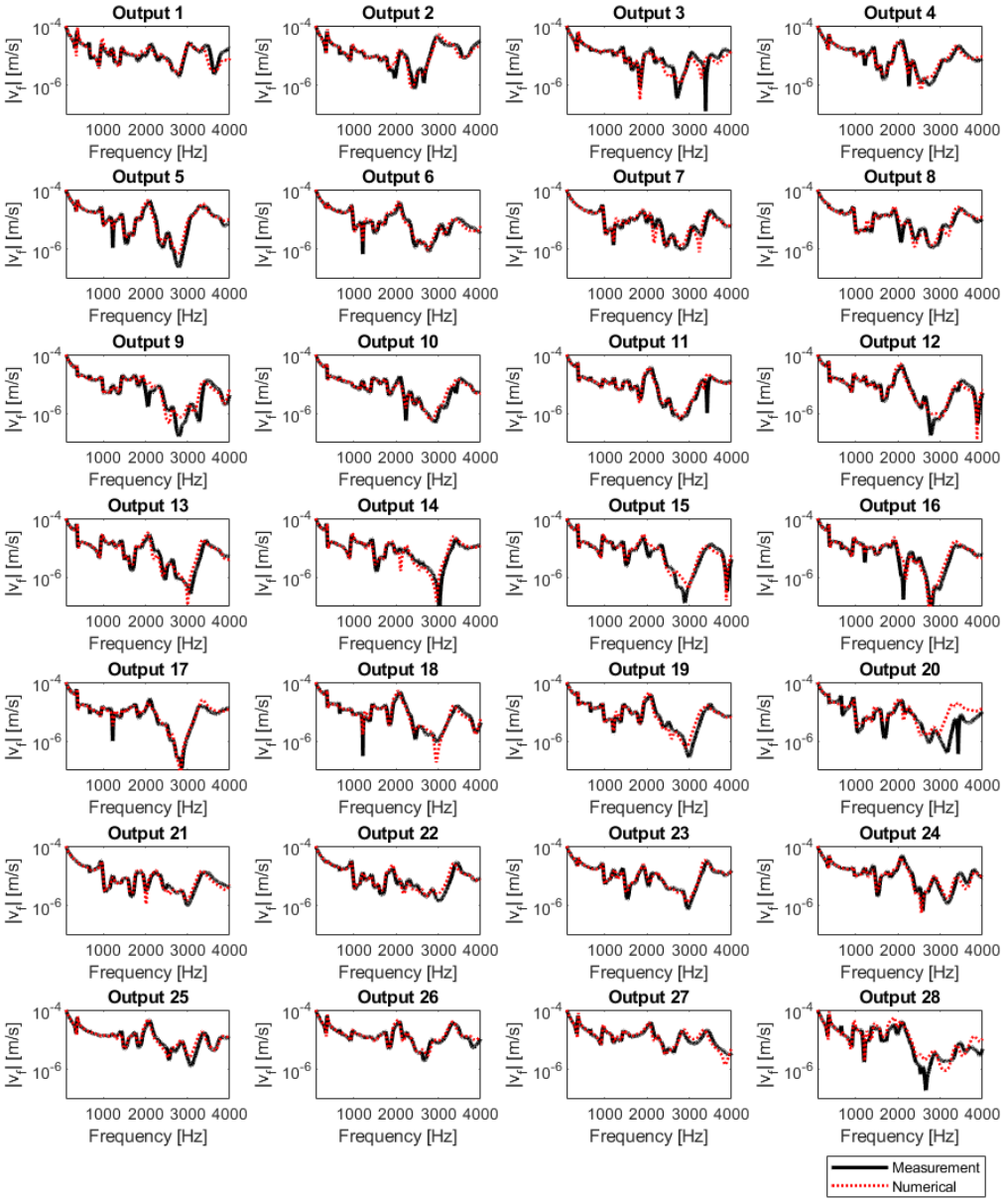

Figure B.18: Numerical and measured velocity at every output point for the optimized case, obtained by summing up all velocities at that point over the different excitation points.

References

[1] F. Fahy, P. Gardonio, Sound and structural vibration: radiation, transmission and response, 2nd edition, Elsevier, UK, 2007.

[2] J. R. Vinson, Sandwich structures, Appl. Mech. Rev. 54 (3) (2001) 201–214.

[3] V. D'Alessandro, G. Petrone, F. Franco, S. De Rosa, A review of the vibroacoustics of sandwich panels: Models and experiments, Journal of Sandwich Structures & Materials 15 (5) (2013) 541–582.

[4] Q. Li, D. Yang, Mechanical and acoustic performance of sandwich panels with hybrid cellular cores, Journal of Vibration and Acoustics 140 (6), https://doi.org/10.1115/1.4040514.

[5] V. Cool, O. Sigmund, N. Aage, F. Naets, E. Deckers, Vibroacoustic topology optimization for sound transmission minimization through sandwich structures, J. of Sound and Vibr. 568 (2024) 117959, https://doi.org/10.1016/j.jsv.2023.117959.

[6] M. Arunkumar, J. Pitchaimani, K. Gangadharan, M. L. Babu, Influence of nature of core on vibro acoustic behavior of sandwich aerospace structures, Aerospace Science and Techn. 56 (2016) 155–167.

[7] M. H. Asadi Jafari, M. Zarastvand, J. Zhou, Doubly curved truss core composite shell system for broadband diffuse acoustic insulation, Journal of Vibration and Control (2023) 10775463231206229.

[8] R. Talebitooti, M. Zarastvand, The effect of nature of porous material on diffuse field acoustic transmission of the sandwich aerospace composite doubly curved shell, Aerospace Science and Technology 78 (2018) 157–170.

[9] N. Guenfoud, C. Droz, M. N. Ichchou, O. Bareille, E. Deckers, W. Desmet, On the multi-scale vibroacoustic behavior of multi-layer rectangular core topology systems, Mechanical Systems and Signal Processing 143 (2020) 106629.

[10] F. Errico, M. Ichchou, S. De Rosa, F. Franco, O. Bareille, Investigations about periodic design for broadband increased sound transmission loss of sandwich panels using 3d-printed models, Mech. Syst. Signal Proc. 136 (2020) 106432.

[11] M. A. Lang, C. L. Dym, Optimal acoustic design of sandwich panels, J. of the Acoust. Soc. of America 57 (6) (1975) 1481–1487, https://doi.org/10.1121/1.380588.

[12] L. Ren, H. Yang, L. Liu, C. Zhai, Y. Song, Sound insulation of corrugated-core sandwich panels: Modeling, optimization and experiment, Materials 14 (24) (2021) 7785, https://doi.org/10.3390/ma14247785.

[13] A. Hosseinkhani, D. Younesian, A. O. Krushynska, M. Ranjbar, F. Scarpa, Full-gradient optimization of the vibroacoustic performance of (non-) auxetic sandwich panels, Transp. in Porous Media 142 (1) (2022) 139–156, https://doi.org/10.1007/s11242-021-01693-0.

[14] H. Denli, J. Sun, Structural-acoustic optimization of sandwich structures with cellular cores for minimum sound radiation, J. Sound Vibr. 301 (1-2) (2007) 93–105, https://doi.org/10.1016/j.jsv.2006.09.025.

[15] H. Yang, H. Li, H. Zheng, A structural-acoustic optimization of two-dimensional sandwich plates with corrugated cores, J. Vibr. Control 23 (18) (2017) 3007–3022.

[16] L. Shu, M. Y. Wang, Z. Ma, Level set based topology optimization of vibrating structures for coupled acoustic–structural dynamics, Computers & Struct. 132 (2014) 34–42, https://doi.org/10.1016/j.compstruc.2013.10.019.

[17] W. M. Vicente, R. Picelli, R. Pavanello, Y. M. Xie, Topology optimization of periodic structures for coupled acoustic-structure systems, in: VII European congress on comput. methods in appl. sciences and eng., 2016.

[18] J. Hu, S. Yao, X. Huang, Topological design of sandwich structures filling with poroelastic materials for sound insulation, Finite Elements in Analysis and Design 199 (2022) 103650, https://doi.org/10.1016/j.finel.2021.103650.

[19] Y. Wang, H. Zhao, H. Yang, J. Liu, D. Yu, J. Wen, Topological design of lattice materials with application to underwater sound insulation, Mech. Syst. and Signal Process. 171 (2022) 108911, https://doi.org/10.1016/j.ymssp.2022.108911.

[20] J. Jewett, J. Carstensen, Topology-optimized design, construction and experimental evaluation of concrete beams, Automation in Constr. 102 (2019) 59–67, https://doi.org/10.1016/j.autcon.2019.02.001.

[21] B. Liu, L.and Yi, T. Wang, Z. Li, J. Zhang, G. Yoon, Investigation on numerical analysis and mechanics experiments for topology optimization of functionally graded lattice structure, Additive Manuf. 47 (2021) 102275, https://doi.org/10.1016/j.addma.2021.102275.

[22] Z. Zhao, C. Wang, X. Zhang, Tuning buckling behaviors in magnetically active structures: topology

optimization and experimental validation, J. of Appl. Mech. 90 (9), https://doi.org/10.1115/1.4062536.

[23] K. Hirasawa, I. Nakami, T. Ooinoue, T. Asaoka, G. Fujii, Experimental demonstration of thermal cloaking metastructures designed by topology optimization, Int. J. of Heat and Mass Transfer 194 (2022) 123093, https://doi.org/10.1016/j.ijheatmasstransfer.2022.123093.

[24] Y. Hua, C. Qian, H. Chen, H. Wang, Experimental topology-optimized cloak for water waves, Mat. Today Phys. 27 (2022) 100754, https://doi.org/10.1016/j.mtphys.2022.100754.

[25] J. Guo, X. Zhang, Y. Fang, Topology optimization design and experimental validation of an acoustic metasurface for reflected wavefront modulation, J. of Sound and Vibr. 520 (2022) 116631, https://doi.org/10.1016/j.jsv.2021.116631.

[26] I. 140-4:1998, Acoustics — measurement of sound insulation in buildings and of building elements — part 4: Field measurements of airborne sound insulation between rooms, ISO/TC 43/SC 2 Building acousticshttps://www.iso.org/standard/2210.html.

[27] A. Cops, M. Minten, Comparative study between the sound intensity method and the conventional two-room method to calculate the sound transmission loss of wall construction, Noise control engineering journal 22 (3) (1984) 104–111.

[28] M. J. Bell, An application of fast fourier transform processing to the measurement of sound transmission loss, Ph.D. thesis, UNSW Sydney (1977).

[29] P. Schomer, Measurement of sound transmission loss by combining correlation and fourier techniques, The J. of the Acoust. Soc. of Am. 51 (4A) (1972) 1127–1141.

[30] A. S. E1050-19, Standard test method for impedance and absorption of acoustical materials using a tube, two microphones and a digital frequency analysis system, ASTM Internationalhttps://www.astm.org/e1050-19.html.

[31] M. Akoum, J.-M. Ville, Measurement of the reflection matrix of a discontinuity in a duct, The Journal of the Acoustical Society of America 103 (5) (1998) 2463–2468, https://doi.org/10.1121/1.422766.

[32] Z. Zhang, H. Denayer, C. Claeys, W. Desmet, E. Deckers, Angle-dependent reflection, transmission and absorption coefficients measurement using a 2D waveguide, Appl. Acoust. 177 (2021) 107946, https://doi.org/10.1016/j.apacoust.2021.107946.

[33] R. F. Boukadia, E. Deckers, C. Claeys, M. Ichchou, W. Desmet, A wave-based optimization framework for 1D and 2D periodic structures, Mech. Syst. and Signal Process. 139 (2020) 106603, https://doi.org/10.1016/j.ymssp.2019.106603.

[34] F. Bloch, Über die quantenmechanik der elektronen in kristallgittern, Z. für Phys. 52 (7) (1929) 555–600, https://link.springer.com/article/10.1007/BF01339455.

[35] M. Hussein, M. Leamy, M. Ruzzene, Dynamics of phononic materials and structures: Historical origins, recent progress, and future outlook, Appl. Mech. Rev. 66 (4) (2014) 040802, https://doi.org/10.1115/1.4026911.

[36] N. de Melo Filho, L. Van Belle, C. Claeys, E. Deckers, W. Desmet, Dynamic mass based sound transmission loss prediction of vibro-acoustic metamaterial double panels applied to the mass-air-mass resonance, J. Sound Vibr. 442 (2019) 28–44, https://doi.org/10.1016/j.jsv.2018.10.047.

[37] J. Jensen, A simple method for coupled acoustic-mechanical analysis with application to gradient-based topology optimization, Struct. and Multidiscipl. Opt. 59 (5) (2019) 1567–1580, https://doi.org/10.1007/s00158-018-2147-4.

[38] F. Wang, B. S. Lazarov, O. Sigmund, On projection methods, convergence and robust formulations in topology optimization, Struct. and Multidiscipl. Opt. 43 (6) (2011) 767–784, https://doi.org/10.1007/s00158-010-0602-y.

[39] V. Cool, L. Van Belle, C. Claeys, W. Desmet, E. Deckers, Impact of the acoustic transmission path on the vibro-acoustic performance of sandwich panels with structural cores with bandgap behavior, Appl. Acoust. 200 (2022) 109080, https://doi.org/10.1016/j.apacoust.2022.109080.

[40] S. Ehsan Moosavimehr, A. Srikantha Phani, Sound transmission loss characteristics of sandwich panels with a truss lattice core, The J. of the Acoust. Soc. of America 141 (4) (2017) 2921–2932, https://doi.org/10.1121/1.4979934.

[41] B. Mace, E. Manconi, Wave motion and dispersion phenomena: Veering, locking and strong coupling effects, The J. of the Acoust. Soc. of Am. 131 (2) (2012) 1015–1028, https://doi.org/10.1121/1.3672647.

[42] C. W. Isaac, M. Pawelczyk, S. Wrona, Comparative study of sound transmission losses of sandwich composite double panel walls, Appl. Sciences 10 (4) (2020) 1543.

[43] F. Franco, S. De Rosa, T. Polito, Finite element investigations on the vibroacoustic performance of plane plates with random stiffness, Mech. Adv. Mat. Struct. 18 (7) (2011) 484–497.

[44] R. E. Christiansen, B. S. Lazarov, J. S. Jensen, O. Sigmund, Creating geometrically robust designs for highly sensitive problems using topology optimization, Struct. and Multidiscipl. Opt. 52 (4) (2015) 737–754, https://doi.org.10.1007/s00158-015-1265-5.

[45] D. Fritze, S. Marburg, H.-J. Hardtke, Estimation of radiated sound power: A case study on common approximation methods, Acta Acustica united with Acustica 95 (5) (2009) 833–842, https://doi.org/10.3813/AAA.918214.

[46] J. Jung, J. Kook, S. Goo, S. Wang, Sound transmission analysis of plate structures using the finite element method and elementary radiator approach with radiator error index, Adv. in Eng. Software 112 (2017) 1–15, https://doi.org/10.1016/j.advengsoft.2017.06.001.

[47] G. Koopmann, J. Fahnline, Designing quiet structures: a sound power minimization approach, Elsevier, 1997.

[48] Y. Yang, M. Kingan, B. Mace, A wave and finite element method for calculating sound transmission through rectangular panels, Mech. Syst. and Signal Proc. 151 (2021) 107357, https://doi.org/10.1016/j.ymssp.2020.107357.

[49] Y. Yang, B. Mace, M. Kingan, Ranking of sound transmission paths by wave and finite element analysis, J. of Sound and Vibr. 492 (2021) 115765, https://doi.org/10.1016/j.jsv.2020.115765.

[50] Y. Yang, B. R. Mace, M. J. Kingan, Prediction of sound transmission through, and radiation from, panels using a wave and finite element method, J. Acoust. Soc. Am. 141 (4) (2017) 2452–2460, https://doi.org/10.1121/1.4977925.

[51] L. Sangiuliano, C. Claeys, E. Deckers, W. Desmet, Influence of boundary conditions on the stop band effect in finite locally resonant metamaterial beams, J. of Sound and Vibr. 473 (2020) 115225, https://doi.org/10.1016/j.jsv.2020.115225.

[52] O. Collery, J.-L. Guyader, Solving the vibroacoustic equations of plates by minimization of error on a sample of observation points, J. Acoust. Soc. Am. 127 (3) (2010) 1347–1356.

[53] B. Bourdin, Filters in topology optimization, Int. J. Num. methods Eng. 50 (9) (2001) 2143–2158, https://doi.org/10.1002/nme.116.

[54] J. K. Guest, J. H. Prévost, T. Belytschko, Achieving minimum length scale in topology optimization using nodal design variables and projection functions, Int. J. Num. Methods Eng. 61 (2) (2004) 238–254, https://doi.org/10.1002/nme.1064.

[55] M. Stolpe, K. Svanberg, An alternative interpolation scheme for minimum compliance topology optimization, Struct. and Multidiscipl. Opt. 22 (2) (2001) 116–124, https://doi.org/10.1007/s001580100129.

[56] K. Svanberg, The method of moving asymptotes—a new method for structural optimization, Int. J. for Num. Methods in Eng. 24 (2) (1987) 359–373, https://doi.org/10.1002/nme.1620240207.